

# Rapid glacier retreat rates observed in West Antarctica

**Authors:** P.Milillo<sup>1,2,4\*</sup>, E.Rignot<sup>2,3,4</sup>, P.Rizzoli<sup>4</sup>, B.Scheuchl<sup>2</sup>, J.Mouginot<sup>2,6</sup>, J.L. Bueso-Bello<sup>4</sup>,  
P.Prats-Iraola<sup>4</sup>, L.Dini<sup>7</sup>

## Affiliations:

<sup>1</sup> Department of Civil & Environmental Engineering, University of Houston, TX, USA

<sup>2</sup> Department of Earth System Science, University of California, Irvine, CA, USA

<sup>3</sup> Department of Civil & Environmental Engineering, University of California, Irvine, CA, USA

<sup>4</sup> German Aerospace Center (DLR), Microwaves and Radar Institute, Munich, Germany

<sup>5</sup> Jet Propulsion Laboratory, California Institute of Technology, Pasadena, CA, USA

<sup>6</sup> Univ. Grenoble Alpes, CNRS, IRD, Grenoble INP, IGE, 38000, Grenoble, France

<sup>7</sup>Italian Space Agency (ASI), Matera, Italy

## Abstracts

The Pope, Smith, and Kohler glaciers, in the Amundsen Sea Embayment of West Antarctica, have experienced enhanced ocean-induced ice-shelf melt, glacier acceleration, ice thinning, and grounding line retreat in the past thirty years. Here we present observations of the grounding line retreat of these glaciers since 2014 using a constellation of interferometric radar satellites combined with precision surface elevation data. We find that the grounding lines develop spatially-variable, kilometre-scale, tidally-induced migration zones. After correction for tidal effects, we detect a sustained pattern of retreat coincident with high melt rates of un-grounded ice, marked by episodes of more rapid retreat. In 2017, Pope Glacier retreated 3.5 km in 3.6 months, or 11.7 km/yr. In 2016-2018, Smith West retreated at 2 km/yr and Kohler at 1.3 km/yr. While the retreat slowed down in 2018-2020, these retreat rates are faster than anticipated by numerical models on yearly time scales. We hypothesize that the rapid retreat is caused by un-represented, vigorous ice-ocean interactions acting within newly-formed cavities at the ice-ocean boundary.

26

27 **Introduction.**

28           The Amundsen Sea Embayment (ASE) sector of West Antarctica, which includes the Pine  
29 Island, Thwaites, Haynes, Pope, Smith and Kohler glaciers, dominates the present-day  
30 contribution to sea level rise from Antarctica (1-2). Their ice volume above flotation is equivalent  
31 to a 1.2-meter global sea level rise. Located on the western flank of the ASE, the Pope, Smith, and  
32 Kohler glaciers drain 7% of the ASE into the Crosson and Dotson ice shelves, but contribute 24%  
33 of the total loss from ASE, with an average 32 Gt/yr mass loss (1 Gt =  $10^9$  ton =  $10^{12}$  kg) during  
34 the time period 1979-2017 (2-3) (Fig. 1). Although their combined ice discharge is 3 times lower  
35 than that of the neighboring Pine Island and Thwaites glaciers, their rapid speed up and retreat  
36 rate, along mostly retrograde bed slopes (i.e. bed elevation drops in the inland direction), are  
37 diagnostic of what an extensive glacier retreat associated with a “marine ice sheet instability” may  
38 look like in the broader remainder of West Antarctica in the future (4).

39           A number of changes were noted in prior studies of these glaciers. At the grounding line -  
40 where ice detaches from the bed and becomes afloat - the velocity of Pope Glacier increased from  
41 370 m/yr in 1989 to 775 m/yr in 2016, which doubled its ice discharge from  $5.5 \pm 0.6$  to  $9.5 \pm 0.7$   
42 Gt/yr (5). Near the grounding line, grounded ice thinned at 9 m/yr between 2003 and 2008 while  
43 floating ice melted at 40 m/yr (6-8). The grounding line retreated at 0.64 km/yr from 1996 to 2014  
44 (5). On Smith East and West, the velocity increased by 280% (710 m/yr) and 370% (800 m/yr),  
45 respectively, in 1992-2015, which tripled their combined ice discharge as the grounding line  
46 retreated into thicker ice (5). Between 2002 and 2009, Smith West thinned at 7 m/yr on grounded  
47 ice and melted at 70 m/yr on floating ice (9). From 1992 to 2016, the grounding line of Smith West  
48 retreated at 2 km/yr, which was the fastest retreat rate in Antarctica (10), while Smith East retreated

49 at 0.5 km/yr. In contrast, Kohler exhibited no speed up between 1994 and 2016 and its grounding  
50 line migrated back and forth between 1996 and 2014 (5).

### 51 **Short-term grounding line variability.**

52 Here we present a new time series of 1-day repeat synthetic aperture radar interferometry  
53 (InSAR) observations from the COSMO-SkyMed (CSK) constellation to survey the Pope, Smith  
54 East and West and Kohler glaciers multiple times a year and update on their grounding line position  
55 since year 2014. We combine the CSK differential InSAR (DInSAR) data (Fig. S1) with time-  
56 tagged TanDEM-X (TDX) digital elevation models (DEM) of the ice surface. The time series of  
57 DInSAR data reveals the temporal evolution of the grounding line caused by tidally-induced  
58 migrations on top of a long-term grounding line retreat (see Methods) (11-12) (Fig. 1). The TDX  
59 DEMs (Fig. S2-3) quantify temporal changes in ice surface elevation caused by changes in ice  
60 flow dynamics and surface mass balance on grounded ice, and additionally by bottom ice melt by  
61 the ocean waters on floating ice (Fig. S3). In the DInSAR technique, we form the difference  
62 between a first 1-day InSAR pair that includes signal associated with the nearly-steady horizontal  
63 motion of the glacier and the tidal-dependent vertical tidal motion of the floating ice with a second  
64 1-day InSAR pair, acquired within 1 to 4 of 16-day cycles later, to eliminate the steady, horizontal  
65 motion of the glacier and detect the residual pattern of tidal motion. The DInSAR technique  
66 combines 4 SAR images from 4 epochs to image a differential pattern of tidal motion. We posit  
67 that the vertical motion detected farthest inland in the DInSAR data corresponds to the most  
68 positive (upward) tide,  $h_{max}$ , among the 4 epochs because the high tide will lift the glacier farther  
69 off the bed and allow seawater to intrude farther inland beneath the glacier, whereas low tide will  
70 force the grounding line to re-advance (12). We model the tidal heights at the time of passage of  
71 the satellites using the Circum-Antarctic Tidal Simulation (CATS2008) (13) and correct the results

72 for changes in atmospheric pressure. We examine the relationship between observed grounding  
73 line position from each DInSAR element and the modeled maximum tide ( $h_{max}$ ) at the time of  
74 passage of the satellites (Fig. 2).

75 We find a larger-than-expected variability in grounding line position as a function of tide.  
76 On Smith West, the grounding line migrates at tidal frequencies over a 3-km wide grounding zone  
77 – where the grounding line migrates with changes in oceanic tide – in 2016-2017. In 1992-1995,  
78 the grounding zone was 1.6 km wide (Fig. 3). The larger tidally-induced grounding zone in 2016-  
79 2017 is consistent with a flatter bed topography at that location (14-15) compared to 1992-1995  
80 (Fig. 3). A flatter topography favors intrusion of pressurized seawater at the glacier bed at high  
81 tide over a larger area. Conversely, the grounding zone will be narrower along steeper parts of the  
82 bed, e.g. along the side margins or at bed peaks (Fig. 1), if tidal migration is controlled by  
83 hydrostatic equilibrium (11-12).

84 We find a positive, linear relationship between observed grounding line position and  
85 modeled maximum tide,  $h_{max}$  (Fig. 2). The slope of the regression varies from glacier to glacier  
86 and is time dependent as the grounding line retreats to a different bed position (Table 1). If we  
87 assume flotation, the sensitivity of the grounding line position to tidal height,  $\gamma$ , is given by the bed  
88 and surface slopes and the density of seawater and ice (See Methods). We find, however, that the  
89 observed grounding line migration is amplified by a factor,  $a$ , that varies from 1 to 37 (Table 1),  
90 i.e. the migration is one order of magnitude larger than expected from flotation. Within the  
91 grounding zones of Pope, Smith and Kohler glaciers, we find that ice deviates from flotation by  
92 only  $3.9 \pm 6$  m,  $2.5 \pm 8$  m, and  $2.2 \pm 6$  m, respectively (Fig. S5).

93 **Long term grounding line migration.**

94 We employ the empirical relationship between grounding line position and tidal height to  
95 derive a mean - or tidal-corrected - position of grounding line at different epochs, and in turn use  
96 these results to determine the longer term (months to years) migration independent of the tidal  
97 state (Fig. 3). We find that the grounding line of Smith East retreated at 1.4 km/yr in 2011-2016  
98 along a relatively flat bed, or 3 times faster than in 1996-2011 (5). The grounding line remained  
99 stable in 2016-2017 at a transition to prograde slopes, followed by a retreat at 2.4 km/yr in 2017-  
100 2018, and a slow down to 0.9 km/yr in 2018-2020 along steeper prograde slopes (Fig. 3). The  
101 grounding line of Smith West retreated  $3.0 \pm 0.4$  km in 2016-2017,  $1.5 \pm 0.4$  km in 2017-2018, and  
102 remained stable in 2018-2020, for an average 0.9 km/year retreat in 2016-2020, or 50% slower  
103 than in 1992-2011 (Fig. 3). During 2014-2020, the retreat proceeded on a nearly flat bed whereas  
104 in 1996-2011 the grounding line retreated along retrograde slopes (600-m drop in elevation in 30  
105 km). On the western flank of Smith West (Point D in Fig. S3), 11 km<sup>2</sup> of grounded ice disappeared  
106 between February 2016 and December 2017, accompanied by a 2.3 km/yr retreat of the grounding  
107 line.

108 To the east, Pope Glacier retreated  $2.7 \pm 0.8$  km in 2014-2016, or 1.3 km/yr, versus 0.6  
109 km/yr in 1994-2014 (5). The grounding zone is only 1 km wide (Fig. 3). In January-May 2017,  
110 over a period of only 113 days, the grounding line retreated  $3.5 \pm 0.8$  km (see Methods), or 11.7  
111 km/yr. The grounding line subsequently retreated at 0.8 km/yr in 2017-2018 and remained stable  
112 in 2018-2020 as the grounding line transitioned to prograde bed slopes which extend another 20  
113 km inland. During 2016-2020, the grounding line average a retreat rate of 1 km/yr.

114 To the west, Kohler Glacier exhibits a 2-km wide grounding zone along prograde bed  
115 slopes (Fig. 3). The grounding line retreated  $2.3 \pm 0.4$  km in 2016-2018 but did not retreat in 2018-  
116 2020, for an average 0.5 km/year retreat in 2016-2020, or 60% higher than in 1995-2016. A prior

117 study suggested a re-advance of the grounding line in 2011-2014 (5). The grounding line now  
118 stands 7 km away from Smith West and 2 km from retrograde slopes. At the current rate, the two  
119 glaciers will merge within the next 15 years. This merger will have two implications. First, the  
120 connection of ice shelf cavities will change the ocean circulation beneath Dotson (16). Second, the  
121 prograde bed slopes of Kohler, which explained its apparent stability in 1992-2014, did not stop  
122 the retreat. Similarly, Smith East retreated slowly along prograde slopes in 2017-2020.

123 Retreat rates of 3 km/yr on Smith West in 2016-2017, 2.4 km/yr on Smith East in 2017-  
124 2018, 11.7 km/yr in 3 months on Pope in 2017, and 2.3 km/yr on Kohler in 2016-2018 are large  
125 compared to those observed on other glaciers in Antarctica and Greenland. The grounding line of  
126 Jakobshavn Isbræ, central west Greenland, retreated at 0.5 km/yr in 2002-2016, with a brief 3.8  
127 km jump in 2011-2012 (17). Zachariae Isstrøm, northeast Greenland, retreated at 0.55 km/yr in  
128 2014-2019 (18-19). Helheim retreated by 4 km between August 2004 and August 2005 (19), but  
129 partially re-advanced in subsequent years. In West Antarctica, Thwaites has retreated at 1 km/yr  
130 on average since 1992, similar to Pine Island (11-12, 21). The observed high retreat rates of Smith,  
131 Pope and Kohler in recent years are however consistent with retreat rates as large as 5 to 10 km/yr  
132 inferred recently for former paleo ice streams (23), giving credence to the fact that glaciers can  
133 retreat at speeds of several km per year.

#### 134 **Ice-ocean interactions in the grounding zones.**

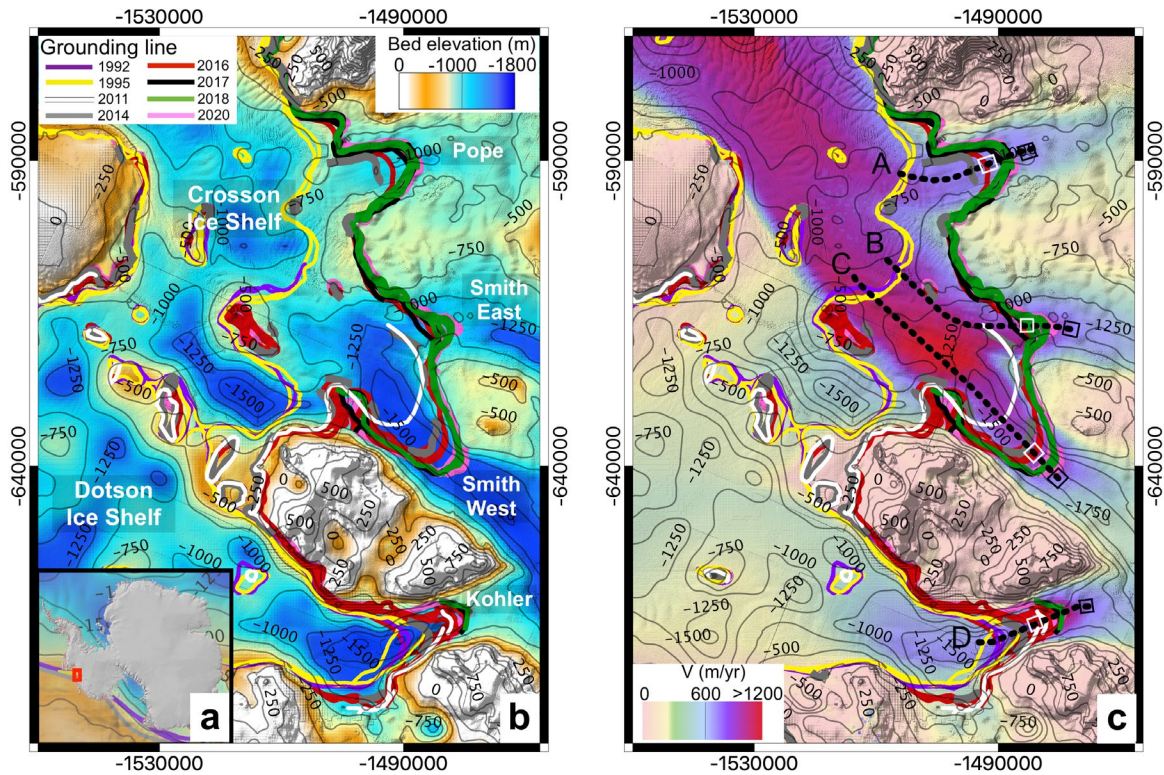
135 The time series of DEMs document the rate of ice thinning accompanying the retreat. The  
136 highest thinning rates are observed in areas of freshly un-grounded ice (6-7) and are caused by a  
137 combination of dynamic thinning and bottom melt by the ocean waters (surface mass balance is  
138 less than 0.5 m/yr in this region (25), hence is not a factor). On land, dynamic thinning equals the  
139 rate of ice thinning, which we calculate over grounded ice adjacent to the freshly un-grounded ice

140 (Fig. 1). We assume that the same rate of dynamic thinning applies on un-grounded ice, subtract  
141 this rate from the observed rate of ice thinning, assume hydrostatic equilibrium, and deduce the  
142 resulting bottom melt rate (See Methods). Ice only deviates from flotation by a few meters due to  
143 bending stresses (11, 24) in these regions. Above the 2020 grounding lines, we detect ice thinning  
144 at 4 to 7 m/yr on Pope, Smith and Kohler glaciers (Fig. 4) and peak values of 9 m/yr on Smith  
145 West in 2011-2014 (Fig. S3). For ice that ungrounded on Pope in 2014-2017, we calculate a bottom  
146 melt rate of  $86 \pm 9$  m/yr (Fig. 4a, Fig. S5, Fig. S6). On Smith East, dynamic thinning of 5 m/yr in  
147 2011-2019 on grounded ice translates into a melt rate of  $22 \pm 6$  m/yr on freshly un-grounded ice  
148 (Fig. 4b). For Smith West, grounded ice thinning at  $6 \pm 0.4$  m/yr yields a  $65 \pm 6$  m/yr melt rate of un-  
149 grounded ice. For Kohler, grounded ice thinning at 3-4 m/yr yields  $19 \pm 7$  m/yr melting of un-  
150 grounded ice. At select locations D-E (Fig. S3) on Smith West, inferred bottom melt rates exceed  
151 100 m/yr, e.g. 140 m/yr in 2016–2017 at D. On Kohler, the melt rate is  $100 \pm 9$  m/yr in 2016-2019  
152 at Point F (Fig. S3). These melt rates are high compared to melt rates observed on the ice shelf  
153 proper (26) and in the upper range of values employed in numerical ice sheet models (9, 27-29).

154         When similar high melt rates are used to force models, the model results can match the  
155 observed retreat, except for Kohler where the modeled grounding line remains stable (9). As noted  
156 in prior studies (9,30), elevated ice melt near the grounding line is an additional constraint on the  
157 speed of retreat. Wider grounding zones are explainable by the presence of a deformable bed (31)  
158 or the propagation of elastic cracks forced by pressurized seawater (32, 33). Intrusion of  
159 pressurized seawater in the sub-glacial cavities will melt grounded ice and reduce basal resistance  
160 (34). Numerical models indicate that the inclusion of ice melt within a grounding zone significantly  
161 increases the speed of retreat (30). Other modeling studies even emphasize that it is not possible  
162 to match the observed retreat if ice melt processes are not included in the grounding zone (9, 28).

163           The Pope, Smith East and West, and Kohler glaciers control a drainage area with an ice  
164 volume above flotation equivalent of 6-cm global sea level rise, which is small, so the risks of  
165 rapid sea level rise from this sector of West Antarctica are low. Yet the physical processes driving  
166 their retreat are the same that operate on neighboring Thwaites and Pine Island, which hold a 1.2  
167 m global sea level rise and may de-stabilize the rest of West Antarctica. Understanding the physical  
168 processes driving the fast retreat of Pope, Smith and Kohler, especially the magnitude of ice melt  
169 in the grounding zones, is therefore critical to explain and reproduce the observed rates of retreat.  
170 The results will in turn help reduce uncertainties in the upper bounds of maximum contribution to  
171 sea level rise from West Antarctica in decades to come.

172



174

175

176

**Figure 1. Pope, Smith East and West, and Kohler glaciers, West Antarctica.** (a) Location map

177

in West Antarctica (red box).

178

(b) Shaded-relief bed elevation color-coded from -1800 m (blue) to

179

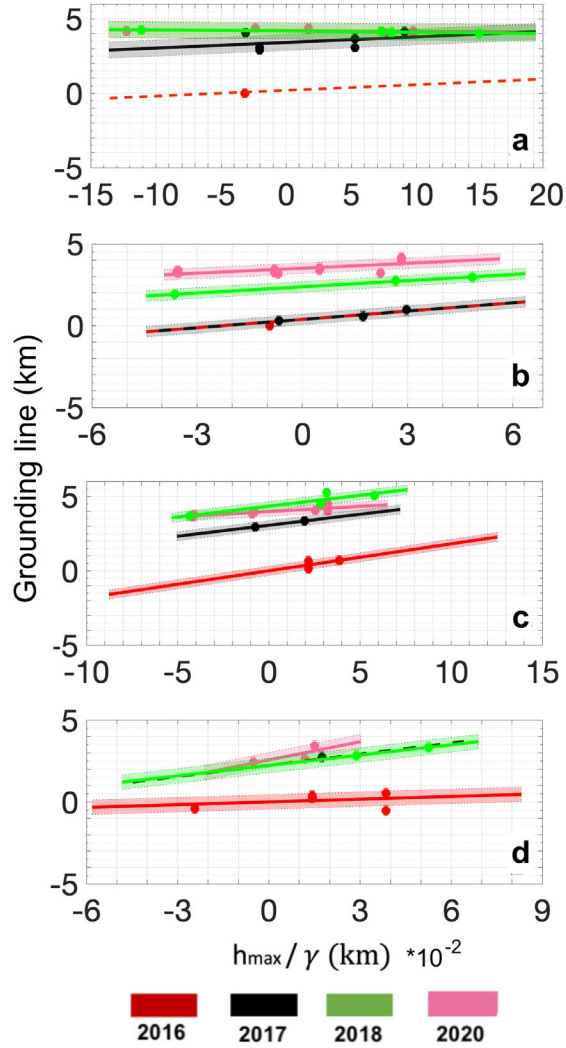
0 m (brown) with 500-m contour levels (grey) (14-15), and grounding zones color coded from

180

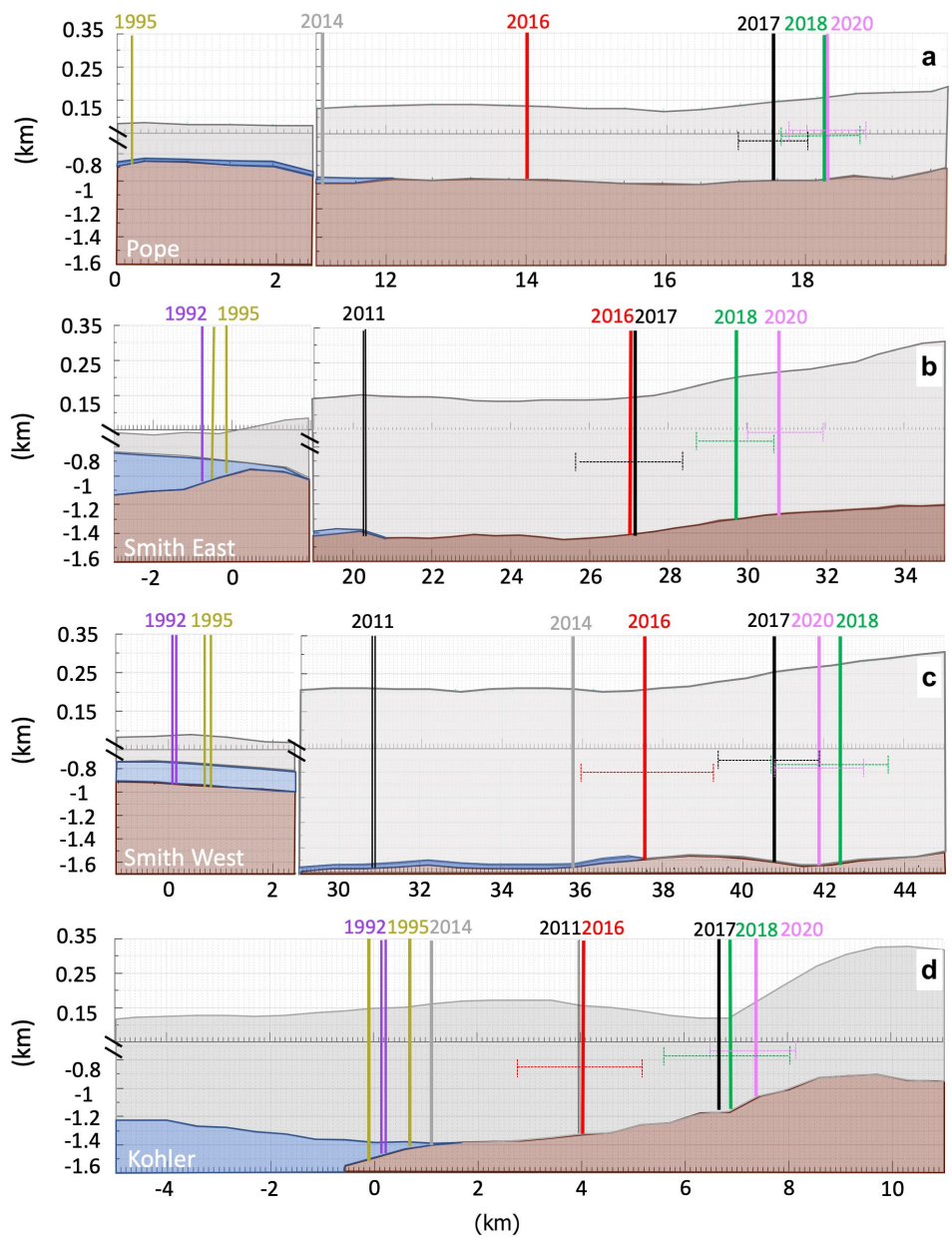
1992 to 2020. Retreat rates are shown in Fig. 2-3 along profiles A-D.

181

(c) Ice surface speed in 2016-2017, color coded from brown to red. Black and white boxes near the 2016 grounding lines are used to calculate dynamic thinning and bottom ice melt in Fig. 4.



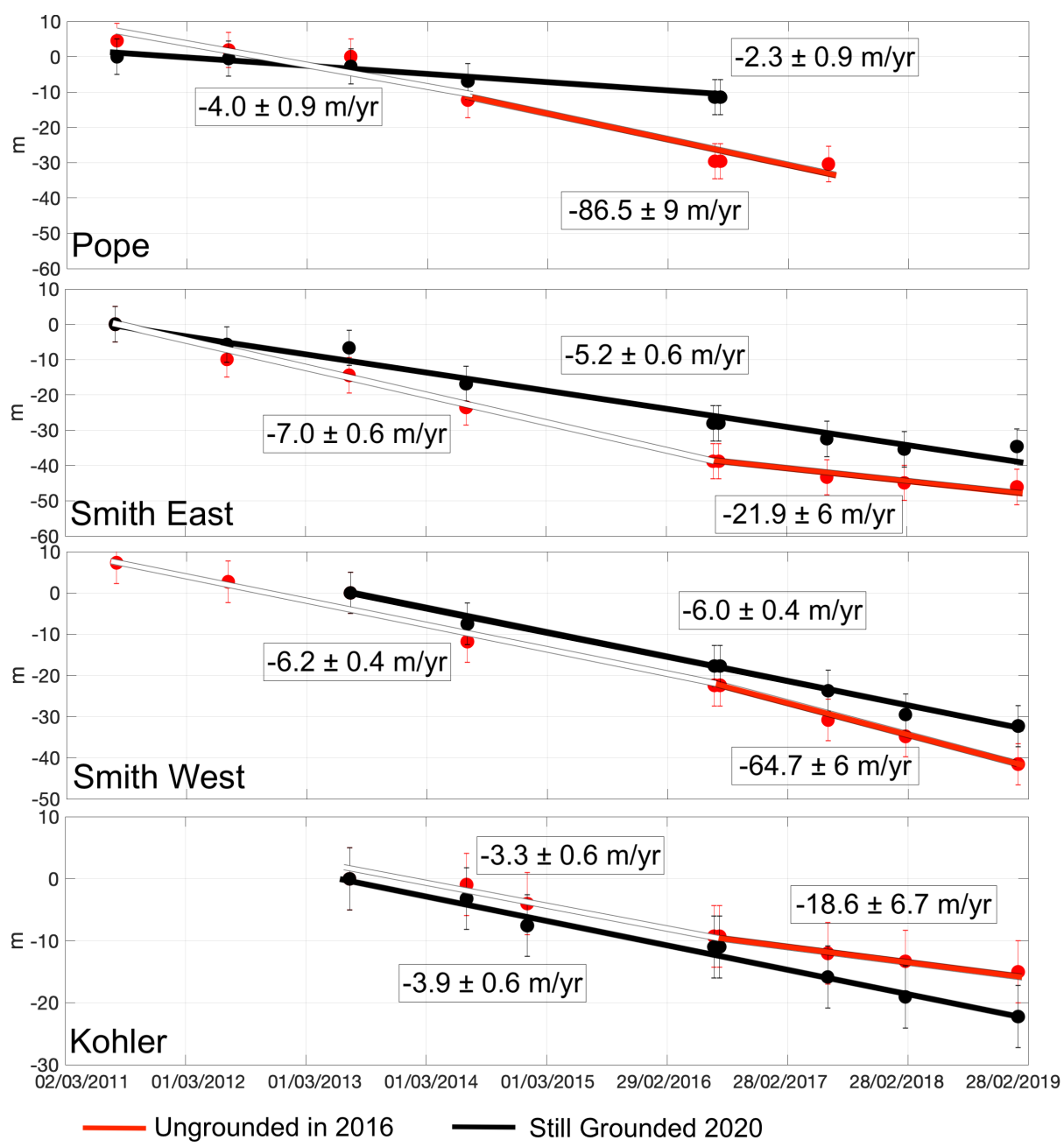
182  
 183 **Figure 2. Tidally-induced grounding line migration (GL) and secular retreat rates at (a) Pope,**  
 184 **(b) Smith East, (c) Smith West and (d) Kohler glaciers as a function of maximum tide,  $h_{max}$ ,**  
 185 **among** the 4 epochs of the DInSAR data divided by the  $\gamma$  values deduced from local, time-dependent,  
 186 **surface and bed slopes (Table 1). GL migration is measured along profiles aligned with the flow**  
 187 **direction and referenced to the 2016 mean-sea-level GL position. Colored lines are linear**  
 188 **regressions of GL versus  $h_{max}/\gamma$ . Shaded areas correspond to a  $1\sigma$  uncertainty. When only one GL**  
 189 **measurement is available for a given year (e.g. Pope and Smith East in 2016/Kohler in 2017), a**  
 190 **dashed red/black line is used assuming the same regression slope as for the nearest available year**  
 191 **(2017 or 2018).**



192  
 193 **Figure 3** Surface and bed profiles of Pope, Smith East, Smith West and Kohler glaciers for  
 194 year 2011 from BedMachine (14) centered at the grounding zone (GZ) of each glacier (Fig. 1).  
 195 Solid colored lines mark the GZ at zero tide and error bars the width of the GZ deduced from Fig.  
 196 2. GZ in 1995, 2011, 2014 from (5) are not corrected for tide due to a limited set of repeat

197 observations. The reference position is the grounding line from the 1990s (Fig. 1). Distance is from  
 198 north (left) to south (right) in km.

199  
 200  
 201



202  
 203

204 **Figure 4. Rate of ice thickness change,  $\frac{dh}{dt_{pre}}$ , and melt rate,  $m_b$ , of West Antarctic glaciers**  
 205 deduced from a time series of TDX digital elevation data corrected for firm depth (Fig. S3). Black  
 206 lines correspond to black boxes in Fig. 1 on grounded ice. White lines correspond to white boxes  
 207 in Fig.1 where ice transitioned from grounded to floating during the time period (marked by a color  
 208 change from white to red). Other examples are shown in Fig. S3 with the same approach.

209  
 210  
 211  
 212 **Table 1.** Sensitivity,  $a$ , of the grounding line position, GL (km), to tidal forcing,  $h_{max}$  (m), for Pope,  
 213 Smith East, Smith West and Kohler glaciers at different times, as a function of surface slope,  $\alpha$ ,  
 214 and bed slope,  $\beta$ , and flotation factor,  $\gamma$ , relative to the 1996 grounding line position (km), and  
 215 grounding zone (GZ) width (km). For ice in hydrostatic equilibrium on a hard bed, we expect the  
 216 sensitivity  $a = GL/(h_{max}/\gamma) = 1$ .

217

<i>Glacier</i>	<i>Time (year)</i>	<i>a</i>	<i>GL retreat (km)</i>	<i><math>\alpha</math> %</i>	<i><math>\beta</math> %</i>	<i><math>\gamma</math></i>	<i>GZ width (km)</i>
<b>Pope</b>	2017	$4.5 \pm 2.1$	$3.5 \pm 0.4$	3	2.7	0.005	$1.5 \pm 0.5$
Lon: -111.59	2018	$1.1 \pm 0.7$	$4.28 \pm 0.4$	3	3	0.005	$1.2 \pm 0.5$
Lat: -75.27	2020	$1.0 \pm 0.7$	$4.25 \pm 0.4$	3	3.5	0.005	$1.4 \pm 0.5$
<b>Smith East</b>	2017	$16.0 \pm 2.1$	$0 \pm 0.4$	1.4	3	0.015	$2.4 \pm 0.5$
Lon: -112.40	2018	$12.5 \pm 2.5$	$2.35 \pm 0.4$	1.4	3	0.015	$1.9 \pm 0.5$
Lat: -75.18	2020	$10.10 \pm 2.1$	$3.25 \pm 0.4$	1.7	2.4	0.018	$1.7 \pm 0.5$
<b>Smith West</b>	2016	$20.1 \pm 10$	$0 \pm 0.3$	0.5	0.4	0.0053	$2.7 \pm 0.5$
Lon: -112.78	2017	$9.8 \pm 6$	$3.0 \pm 0.4$	1.4	1.1	0.014	$2.4 \pm 0.5$
Lat: -75.15	2018	$14.7 \pm 6$	$4.5 \pm 0.4$	1.4	0.8	0.013	$2.4 \pm 0.5$
	2020	$6.1 \pm 6$	$4.0 \pm 0.4$	1.5	0.2	0.013	$2.5 \pm 0.5$
<b>Kohler</b>	2016	$5.6 \pm 4$	$0 \pm 0.5$	0.5	3.3	0.033	$1.9 \pm 0.5$

Lon:-114.17	2018	21.1 ± 7.5	2.3 ±0.4	1.3	3.7	0.015	1.8± 0.5
Lat: -75.10	2020	37.2 ± 7.6	2.5±0.4	3.2	4.2	0.033	1.7± 0.5

218  
219  
220  
221  
222

## References

- 223 (1) Shepherd, A., Ivins, E., Rignot, E., Smith, B., Van Den Broeke, M., Velicogna, I., ... &  
224 Nowicki, S. (2018). Mass balance of the Antarctic Ice Sheet from 1992 to 2017. *Nature*,  
225 **558**, 219-222.
- 226 (2) Rignot, E., Mouginot, J., Scheuchl, B., van den Broeke, M., van Wessem, M. J., &  
227 Morlighem, M. (2019). Four decades of Antarctic Ice Sheet mass balance from 1979–2017.  
228 *Proc. Nat. Acad. Sci.*, **116** (4), 1,095-1,103.
- 229 (3) Mouginot, J., E. Rignot, & B. Scheuchl (2014). Sustained increase in ice discharge from  
230 the Amundsen Sea Embayment, West Antarctica, from 1973 to 2013. *Geophys. Res. Lett.*,  
231 **41**, 1,576-1,584.
- 232 (4) Schoof, C. (2012). Marine ice sheet stability. *J. Fluid Mech.*, **698**, 62-72.
- 233 (5) Scheuchl, B., Mouginot, J., Rignot, E., Morlighem, M., & Khazendar, A. (2016).  
234 Grounding line retreat of Pope, Smith, and Kohler Glaciers, West Antarctica, measured  
235 with Sentinel-1a radar interferometry data. *Geophys. Res. Lett.*, **43**(16), 8,572-8,579.
- 236 (6) Lilien, D. A., Joughin, I., Smith, B., & Shean, D. E. (2018). Changes in flow of Crosson  
237 and Dotson ice shelves, West Antarctica, in response to elevated melt. *The Cryosphere*,  
238 **12**(4), 1,145-1,431.
- 239 (7) Gourmelen, N., Goldberg, D. N., Snow, K., Henley, S. F., Bingham, R. G., Kimura, S., ...  
240 & Ligtenberg, S. R. (2017). Channelized melting drives thinning under a rapidly melting  
241 Antarctic ice shelf. *Geophys. Res. Lett.*, **44**(19), 9,796-9,804.

- 242 (8) Khazendar, A., Rignot, E., Schroeder, D. M., Seroussi, H., Schodlok, M. P., Scheuchl, B.,  
243 & Velicogna, I. (2016). Rapid submarine ice melting in the grounding zones of ice shelves  
244 in West Antarctica. *Nature Comm.*, **7**, ncomms13243.
- 245 (9) Lilien, D. A., Joughin, I., Smith, B., & Gourmelen, N. (2019). Melt at grounding line  
246 controls observed and future retreat of Smith, Pope, and Kohler Glaciers. *The Cryosphere*,  
247 **13**, 2,817-2,834.
- 248 (10) Konrad, H., A. Shepherd, L. Gilbert, A. E. Hogg, M. McMillan, A. Muir & T. Slater  
249 (2018), Net retreat of Antarctic glacier grounding lines. *Nature Geosci.* **11**, 258–262
- 250 (11) Milillo, P., Rignot, E., Rizzoli, P., Scheuchl, B., Mouginot, J., Bueso-Bello, J., & Prats-  
251 Iraola, P. (2019). Heterogeneous retreat and ice melt of Thwaites Glacier, West  
252 Antarctica. *Science Adv.*, **5**(1), eaau3433.
- 253 (12) Milillo, P., Rignot, E., Mouginot, J., Scheuchl, B., Morlighem, M., Li, X., & Salzer, J. T.  
254 (2017). On the short-term Grounding zone dynamics of Pine Island Glacier, West  
255 Antarctica, observed with COSMO-SkyMed Interferometric Data. *Geophys. Res. Lett.*,  
256 **44**(20), 10,436-10,444.
- 257 (13) Padman, L., Fricker, H. A., Coleman, R., Howard, S., & Erofeeva, L. (2002). A new tide  
258 model for the Antarctic ice shelves and seas. *Ann. Glaciol.*, **34**, 247-254.
- 259 (14) Millan, R., E. Rignot, V. Bernier, M. Morlighem, & P. Dutrieux (2017). Bathymetry of  
260 the Amundsen Sea Embayment sector of West Antarctica from operation IceBridge  
261 gravity and other data. *Geophys. Res. Lett.*, **44**, 1,360-1,368.
- 262 (15) Morlighem, M., E. Rignot, T. Binder, D. Blankenship, R. Drew, G. Eagles, O. Eisen, F.  
263 Ferraccioli, R. Forsberg, P. Fretwell, V. Goel, J. S. Greenbaum, H. Gudmundsson, J. Guo,  
264 V. Helm, C. Hofstede, I. Howat, A. Humbert, W. Jokat, N. B. Karlsson, W. S. Lee, K.

265 Matsuoka, R. Millan, J. Mouginot, J. Paden, F. Pattyn, J. Roberts, S. Rosier, A. Ruppel,  
266 H. Seroussi, E. C. Smith, D. Steinhage, B. Sun, M. R. Van Den Broeke, T. D. Van Ommen,  
267 M. Van Wessem, D. Young (2019) Deep glacial troughs and stabilizing ridges unveiled  
268 beneath the margins of the Antarctic ice sheet. *Nature Geosci.*, **13** (2), 132-137.

269 (16) Miles, R., S. H. Lee, A. Wahlin, H. K. Ha, T. W. Kim, K. Assman, & O. Schofield (2016).  
270 Glider observations of the Dotson Ice Shelf outflow. *Deep-Sea Res. II*, **123**, 16-29.

271 (17) An, L., E. Rignot, S. Elieff, M. Morlighem, R. Millan, J. Mouginot, D. M. Holland, D.  
272 Holland, & J. Paden (2017). Bed elevation of Jakobshavn Isbræ, West Greenland, from  
273 high-resolution airborne gravity and other data. *Geophys. Res. Lett.*, **44**(8), 3,728-3,736.

274 (18) Mouginot, J., Rignot, E., Scheuchl, B., Fenty, I., Khazendar, A., Morlighem, & M. Paden,  
275 J. (2015). Fast retreat of Zachariæ Isstrøm, Northeast Greenland. *Science*, **350**(6266),  
276 1,357-1,361.

277 (19) An, L., E. Rignot, M. Wood, J. Willis, J. Mouginot, S. Khan (2021). Ocean melting of the  
278 Zachariæ Isstrøm and Nioghalvfjerdingsfjorden glaciers, northeast Greenland. *Proc. Nat.*  
279 *Acad. Sci.*, 118(2), e2015483118.

280 (20) Howat, I. M., Joughin, I., Tulaczyk, S., & Gogineni, S. (2005). Rapid retreat and  
281 acceleration of Helheim Glacier, east Greenland. *Geophys. Res. Lett.*, 32(22).

282 (21) Rignot, E., Mouginot, J., Morlighem, M., Seroussi, H., & Scheuchl, B. (2014).  
283 Widespread, rapid grounding line retreat of Pine Island, Thwaites, Smith, and Kohler  
284 glaciers, West Antarctica, from 1992 to 2011. *Geophys. Res. Lett.*, **41**(10), 3502-3509.

285 (22) DeConto, R. M., & Pollard, D. (2016). Contribution of Antarctica to past and future sea-  
286 level rise. *Nature*, **531**(7596), 591-597.

- 287 (23) Dowdeswell, J.A., C. L. Batchelor, A. Montelli, D. Ottesen, F. D. W. Christie, E. K.  
288 Dowdeswell, J. Evans. (2020). Delicate seafloor landforms reveal past Antarctic  
289 grounding-line retreat of kilometers per year. *Science*, **368**(6494), 1020-1024.
- 290 (24) Yu, H., E. Rignot, H. Seroussi, M. Morlighem, & Y. Choi (2019). Impact of iceberg  
291 calving on the retreat of Thwaites Glacier, West Antarctica over the next century with  
292 different calving laws and ocean thermal forcing. *Geophys. Res. Lett.*, **46**, 14,539-14,547.
- 293 (25) van Wessem, J. M., van de Berg, W. J., Noël, B. P. Y., van Meijgaard, E., Amory, C.,  
294 Birnbaum, G., Jakobs, C. L., Krüger, K., Lenaerts, J. T. M., Lhermitte, S., Ligtenberg, S.  
295 R. M., Medley, B., Reijmer, C. H., van Tricht, K., Trusel, L. D., van Ulf, L. H., Wouters,  
296 B., Wuite, J., & van den Broeke, M. R. (2018). Modelling the climate and surface mass  
297 balance of polar ice sheets using RACMO2 – Part 2: Antarctica (1979–2016). *The*  
298 *Cryosphere*, **12**, 1,479-1,498.
- 299 (26) Rignot, E., Jacobs, S., Mouginot, J., & Scheuchl, B. (2013). Ice-shelf melting around  
300 Antarctica. *Science*, **341**(6143), 266-270.
- 301 (27) Joughin, I., Smith, B. E., & Medley, B. (2014). Marine ice sheet collapse potentially under  
302 way for the Thwaites Glacier Basin, West Antarctica. *Science*, **344**(6185), 735-738.
- 303 (28) Goldberg, D. N., Gourmelen, N., Kimura, S., Millan, R., & Snow, K. (2019). How  
304 accurately should we model ice shelf melt rates? *Geophys. Res. Lett.*, **46**, 189–199.
- 305 (29) Seroussi, H., Nakayama, Y., Larour, E., Menemenlis, D., Morlighem, M., Rignot, E., &  
306 Khazendar, A. (2017). Continued retreat of Thwaites Glacier, West Antarctica, controlled  
307 by bed topography and ocean circulation. *Geophys. Res. Lett.*, **44**(12), 6191-6199.
- 308 (30) Seroussi H. & M. Morlighem (2018). Representation of basal melting at the grounding  
309 line in ice flow models. *The Cryosphere*, **12**, 3,085–3,096.

- 310 (31) Sayag, R. and M. G. Worster (2013). Elastic dynamics and tidal migration of grounding  
311 lines modify subglacial lubrication and melting. *Geophys. Res. Lett.*, **40**, 5,877–5,881.
- 312 (32) Tsai, V. C., & Gudmundsson, G. H. (2015). An improved model for tidally modulated  
313 grounding-line migration. *J. Glaciol.*, **61**(226), 216-222.
- 314 (33) Begeman, C. B., Tulaczyk, S., Padman, L., King, M., Siegfried, M. R., Hodson, T. O., &  
315 Fricker, H. A. (2020). Tidal pressurization of the ocean cavity near an Antarctic ice shelf  
316 grounding line. *J. Geophys. Res. Oceans*, **125**, e2019JC015562.
- 317 (34) Reese, R., R. Winkelmann, & H. Gudmundsson (2018). Grounding-line flux formula  
318 applied as a flux condition in numerical simulations fails for buttressed Antarctic ice  
319 streams. *The Cryosphere*, **12**(10), 3,229-3,242.
- 320 (35) Rizzoli, P., Martone, M., Gonzalez, C., Wecklich, C., Tridon, D. B., Bräutigam, B., ... &  
321 Wessel, B. (2017). Generation and performance assessment of the global TanDEM-X  
322 digital elevation model. *ISPRS J. Photogram. Rem. Sens.*, **132**, 119-139.
- 323 (36) Padman, L., King, M., Goring, D., Corr, H., & Coleman, R. (2003). Ice-shelf elevation  
324 changes due to atmospheric pressure variations. *J. Glaciol.*, **49**(167), 521-526.
- 325 (37) Berrisford, P., Dee, D., Poli, P., Brugge, R., Fielding, K., Fuentes, M., ... & Simmons, A.  
326 (2011). The ERA-Interim archive, version 2.0.

327

328 **Methods**

329 **COSMO-SkyMed (CSK) grounding line analysis:** We survey the Pope, Smith and Kohler  
330 glaciers grounding lines using the COSMO-SkyMed (CSK) constellation. The acquisition  
331 campaign includes two phases: at the time of phase one (2016-2018), CSK included 4 low-orbit  
332 satellites carrying an X band SAR (3.1 cm wavelength) at HH polarization (horizontal transmit  
333 and receive). Each satellite has a 16-day repeat cycle. Shorter temporal baselines are achieved  
334 using the constellation. We use interferometric acquisitions spanning 1-day time interval with the  
335 satellites CSK2 and CSK3 (Fig. S4). In 2019 no data could be acquired due to a change in satellites  
336 configuration and the addition of 4 more satellites, including 2 X-band COSMO-SkyMed second  
337 generation (CSG) and 2 SAOCOM satellites at L-Band. Phase two started in 2020 and acquisition  
338 spanning 1-day intervals restarted using the CSK2 and CSK4 satellites (Fig. S4). Here, we analyze  
339 scenes in single-look complex (SLC) mode covering a  $40 \times 40$  km swath from 3 different tracks,  
340 at 3 m spacing in the azimuth (along-track) and range (cross-track) directions. CSK SAR  
341 interferograms are assembled by concatenating  $4 \times$  CSK STRIPMAP consecutive frames. The  
342 incidence angle averages  $21^\circ$  across the swath. We apply 8 looks (number of elements averaged  
343 together to reduce noise) in both the range and azimuth directions to improve phase coherence.  
344 We use orbit information and pixel offsets to maximize coherence between image pairs. Given  
345 the large interferometric baseline characterizing CSK2/3 interferometric pairs, we remove the  
346 topographic component of the interferometric phase using time-tagged TDX DEMs acquired  
347 closest in time with the CSK data (11). The interferometric baseline is much reduced in phase 2 of  
348 this project (less than 100 m), in which case we used the same TDX DEM from 2019 with all data.  
349 A grounding line measurement is formed by the differencing two 1-day interferograms. We use  
350 216 stripmap data (an average of 54 SLC per year) divided in 3 tracks (18 images composed by 4

351 frames per image) acquired between February 2016 and November 2020 to produce 26 differential  
 352 interferograms (DInSAR) which reveal vertical tidal displacements and other transient motion of  
 353 the ice, e.g. subsidence/rise of the ice surface with lake drainage/filling (Fig. S1). The precision of  
 354 detection of the grounding line is greater when the differential tidal signal is larger and typically  
 355 of the order of 100-200 meters (11-12). We select 22 DInSAR pairs (85% of the total number of  
 356 pairs) (Fig. S1) that display sufficient tidal signal (i.e. differential tidal signal larger than 4.5 cm  
 357 corresponding to 3 interferometric fringes in the LOS at X band), acquired no more than 2 months  
 358 apart to avoid contaminating the vertical signal with seasonal velocity changes. The grounding line  
 359 is manually picked near the most inland interferometric fringe associated with tidal motion. We  
 360 verify that in each DInSAR frame we count the same number of fringes across the flexure zone,  
 361 i.e. the zone of concentrated fringes where ice adjusts to hydrostatic equilibrium across the  
 362 grounding line. Using multiple grounding line measurements, we identify a grounding zone, i.e.  
 363 where the grounding line migrates back and forth with changes in oceanic tide (Fig. S1).  
 364 One grounding line measurement combines data acquired at 4 different times. We expect the  
 365 grounding line to migrate inland at high tide and seaward at low tide. We posit that the most  
 366 retreated position of the grounding line corresponds to the most positive (upwards) tidal  
 367 displacement among the 4 epochs,  $h_{max}$ . We calculate the tidal amplitude using tide predictions  
 368 from the CATS2008 model with a precision of 5 cm (13)(Table S1). Inverse barometer effect is  
 369 also taken into consideration following the same approach described in (36) using ERA-INTERIM  
 370 data (37)(Table S2). Across the grounding zone, we calculate an average surface slope,  $\alpha$ , from  
 371 the TDX DEM, and a bed slope,  $\beta$ , from BedMachine Antarctica (13-14) along the flow direction  
 372 (Fig. S3) with a length scale of 3 km and calculate a sensitivity parameter  $\gamma$  as:

$$373 \quad (38) \quad \gamma = \left(1 - \frac{\rho_i}{\rho_w}\right)\beta + \frac{\rho_i}{\rho_w}\alpha \quad (\text{Eq. 1})$$

374 where  $\rho_i = 917 \text{ kg m}^{-3}$  and  $\rho_w = 1027 \text{ kg m}^{-3}$  are, respectively, the density of ice and seawater.  
 375 At flotation, when the tide changes by  $dh^+$ , the grounding line should migrate inland by  $dGL$   
 376  $= dh^+/\gamma$  on a rigid bed based on hydrostatic equilibrium (i.e. with  $dh^+ = 1 \text{ m}$  and  $\gamma=0.01$  we  
 377 expect  $dGL$  to be 100 m). The most inland position of the grounding line verifies,  $dGL_{max} =$   
 378  $h_{max} / \gamma$ . In reality, however, because of visco-elastic bed deformation and tidal pressure (30-  
 379 31), the migration is amplified by a factor  $a$ :  $dGL_{max} = a h_{max} / \gamma$  (Fig. 2). The inferred values of  
 380 the amplification factor,  $a$ , are listed in Table 1.

381  
 382 **TanDEM-X DEM (TDX) Bed topography and height above flotation in Antarctica:** We  
 383 generate a time series of 241 time-tagged DEMs using the global TDX product (35) for  
 384 geocoding and calibration for the time period 2011-2019. The SAR processing chain  
 385 comprises 6 steps: 1) spaceborne monostatic TerraSAR-X processing, 2) bistatic TDX  
 386 processing, 3) interferometric combination of images, 4) phase unwrapping, 5) phase-to-  
 387 height conversion and 6) geocoding to a latitude/longitude grid. Using Airborne Topographic  
 388 Mapper (ATM) data over grounded ice, we estimate a relative height accuracy of 2.1 m (Fig.  
 389 S2). For calculating the height above flotation,  $h_f$ , we use surface elevation above mean sea  
 390 level,  $h_{dem}$ , and ice-equivalent thickness,  $H_i$ , from BedMachine Antarctica (14-15) that  
 391 combines ice thickness derived from airborne radar depth sounders with InSAR-derived ice  
 392 velocity and RACMO2.3 surface mass balance data (25). On floating ice, the surface  
 393 elevation of BedMachine Antarctica,  $h_{dem}$ , is corrected with a firn densification,  $d$ , that is  
 394 calibrated with all available ice shelf thickness data. The height above flotation,  $h_f$ , is:

395 
$$h_f = h_{dem} - H_i \left(1 - \frac{\rho_i}{\rho_w}\right) - d \quad (\text{Eq. 2})$$

396 The error in  $h_f$  is 6 m based on an uncertainty of 2 m for  $h_{dem}$ , 50 m in  $H_i$  and 2 m for the firm  
 397 depth,  $d$ , which is optimized so  $h_f \sim$  zero on the ice shelf proper.

398  
 399 **Ice Shelf melt rate:** Time series of surface elevation and grounding line position allow us to  
 400 calculate the ice shelf melt rates,  $m_b$ . From the time series of height above floatation, we  
 401 identify the time when  $h_f$  crosses 0 m and calculate the slope of change in elevation when ice  
 402 is grounded,  $dh/dt_{gd}$ , and after ice becomes afloat,  $dh/dt_{fl}$ . A comparison of  $h_f$  with the  
 403 grounding line position helps gain confidence in the detection of the transition to floatation.  
 404  $dh/dt_{gd}$  is the thinning rate of grounded ice due to ice dynamics.  $dh/dt_{fl}$  is the thinning rate of  
 405 floating ice or recently un-grounded ice, which includes dynamic thinning and ice shelf melt.  
 406 The ice shelf melt,  $m_b$ , is deduced from the difference between these quantities:

$$407 \quad (39) \quad \frac{dh}{dt_{gd}} = \nabla(\mathbf{u} \cdot h) + m_s \quad (\text{Eq. 3})$$

$$408 \quad \frac{dh}{dt_{fl}} = [\nabla(\mathbf{u} \cdot h) + m_s + m_b] / f \quad (\text{Eq. 4})$$

$$409 \quad m_b = f \frac{dh}{dt_{fl}} - \frac{dh}{dt_{gd}} \quad (\text{Eq. 5})$$

410 where  $h$  is the surface elevation,  $m_s$  is the surface mass balance,  $\mathbf{u}$  is the depth-averaged  
 411 velocity, and  $f = \rho_w / (\rho_w - \rho_i) \sim 9.33$  is a flotation factor deduced from the densities of ice and  
 412 seawater. We assume that dynamic thinning does not change rapidly in space as ice un-grounds  
 413 over length scales of a few ice thickness. We confirm this by verifying that the grounded ice  
 414 thinning rate in a box adjacent to the 2020 grounding line is similar to that calculated in a  
 415 nearby box on ice that becomes un-grounded during the observation period (Fig. 1, 4). This  
 416 Eulerian framework, based on the change in elevation at a fixed point in space, reveals how  
 417 rapidly ice melts as the grounding line retreats and ice is exposed to warm ocean waters.

418 **Corresponding Author:** Pietro Milillo, University of Houston, TX – USA, [pmilillo@uh.edu](mailto:pmilillo@uh.edu)

419

420 **Acknowledgments: Funding:** This work was conducted at the UC Irvine under a contract with  
421 the Cryosphere Program of NASA (17-CRYO17-0025, 80NSSC18M0083, and NNX17AI02G).

422 E.R. acknowledges support from the NSF (F0691-04). Author contributions: P.M. set up the

423 CSK Antarctica experiment and acquisition plans and processed and analyzed the CSK data.

424 P.R., P.P.-I., and J.B.-B. processed the TDX time-tagged DEMs. P.M. and E.R. interpreted the

425 results and wrote the manuscript. L.D. Provided support with the CSK data. All authors reviewed

426 the manuscript. Competing interests: The authors declare no competing interest.

427

428 **Data and materials availability:** All data needed to evaluate the conclusions in the paper are

429 present in the paper and/or Supplementary Material. We thank the Italian Space Agency (ASI) for

430 providing CSK data [original COSMO-SkyMed product ASI, Agenzia Spaziale Italiana (2007–

431 2020) and the German Space Agency (DLR) for providing TDX data (original TanDEM-X product

432 DLR (2007–2019)]. CSK data are publicly available through data grants from ASI. TanDEM-X

433 CoSSC products were through scientific proposal OTHER0103 and are publically available.

434 Velocity (<https://nsidc.org/data/NSIDC-0484/versions/2>) and bed machine

435 (<https://nsidc.org/data/NSIDC-0756/versions/2>) data products are available as MEaSURES

436 products at the National Snow and Ice Data Center, Boulder CO (NSIDC). Geocoded

437 interferograms, grounding line positions, reference surface elevation, reference ice thickness,

438 reference height above flotation, and reference ice velocity are available at

439 <https://doi.org/10.7280/D1B114>.

440